Exp Fluids (2011) 50:1235–1245
DOI 10.1007/s00348-010-0969-y

RESEARCH ARTICLE

# A two-color optical method for determining layer thickness in two interacting buoyant plumes

**Yeping Yuan · Margaret E. Avener · Alexander R. Horner-Devine**

Received: 15 September 2009 / Revised: 1 August 2010 / Accepted: 21 August 2010 / Published online: 7 October 2010


**Abstract** We describe a technique for measuring the layer thickness of two interacting buoyant rotating gravity currents. The technique can be used generally to differentiate between water masses in experiments with multiple sources and is used here to simulate the dynamics of two adjacent coastal river plumes. The plumes are generated using two identical fresh water inlets, with blue and red dye indicating upstream and downstream river flows, respectively. Two parameters, normalized intensity and color ratio, are measured with a 3-CCD color video camera and used to develop a two-dimensional (intensity–color ratio) calibration map for layer thickness. The calibration is used successfully to determine the depth field for the combined two-plume system and to differentiate between the two plumes. This technique is applied to compute the volumetric growth of a large eddy near the freshwater source and the transport rate of buoyant fluid away from the source in the coastal current. The validation tests show good agreement between the calculated plume volume and the input fresh water volume.

## 1 Introduction

When buoyant fluid is released near a vertical wall in a rotating system, Coriolis forces guide the density-driven flow along the wall (Griffiths and Hopfinger 1983). If the buoyant fluid is introduced with initial velocity normal to the wall, it forms a two-part structure, with an anticyclonic bulge at the river mouth and a coastal current propagating downstream (in the Kelvin wave sense, i.e., to the right in the northern hemisphere). This bulge circulation has been observed at the mouths of the Columbia River (Horner-Devine 2009) and the Hudson River (Chant et al. 2008). Nof and Pichevin (2001) suggested that the Coriolis force associated with offshore bulge growth balances the alongshore current momentum flux. In the absence of such bulge growth, the alongshore momentum cannot be balanced. A number of previous studies confirm the existence of an unsteady bulge using numerical models (e.g. Fong and Geyer 2002) and laboratory experiments (e.g. Avicola and Huq 2002; Horner-Devine et al. 2006). In the presence of an alongshore ambient current, the river plume can evolve to steady state in which the source freshwater is carried entirely in the coastal current and the bulge growth ceases (Fong and Geyer 2002). In the two-river system, the coastal current from the upstream river act as the non-uniform ambient current to the downstream plume, with a high velocity inshore and almost zero velocity offshore. The primary motivation for experiments described here is to test whether the downstream river bulge remains steady with extra alongshore momentum from the upstream plume.

Many advanced techniques have been applied to measure velocity and/or concentration fields in river plumes. One recent method combines particle image velocimetry (PIV) and planar laser-induced fluorescence (PLIF) to measure two-dimensional velocity and concentration fields simultaneously (e.g. Cowen et al. 2001; Horner-Devine 2006). However, neither PIV nor PLIF is ideally suited for measuring the bulge growth rate since they only resolve a single plane for the plume instead of the entire plume volume. The scanning LIF method provides both time-dependent and space-dependent concentration fields of the buoyant plume (Tian and Roberts 2003). This three-dimensional concentration field could be used to measure

Y. Yuan (✉) · M. E. Avener · A. R. Horner-Devine
Civil and Environmental Engineering,
University of Washington, Seattle, WA, USA
e-mail: yyping@u.washington.com

the bulge volume growth rate, but introduces significant experimental complexity.

Optical thickness measurements can be used to determine plume volume, and thus, the bulge growth rate, from a measured depth field with a relatively simple experimental setup. In the optical thickness method, the thickness of a dyed layer of fluid is measured by illuminating the fluid from beneath and relating the measured intensity (Cenedese 1998), chromaticity (Afanasyev et al. 2009), or saturation (Zhang et al. 1996) to the thickness of the dyed fluid. This method has been applied to measure layer thickness in a number of two-layer systems (Linden and Simpson 1994; Holford and Dalziel 1996; Cenedese 1998). Afanasyev et al. (2009) used a wedged-shaped cuvette filled with the same concentration of dyes to calibrate the layer thickness and then calculated the complete (both time and space dependent) depth field in a rotating fluid.

In our experiments, we need to determine the fresh layer volume and also differentiate between fluids originating from the two different freshwater sources. For this purpose, we extend the existing one color optical thickness method to two colors. The relationship between intensity and thickness depends on the dye color, since attenuation coefficients are different for different dyes. To account for this, we determine a color-specific thickness calibration and apply it differentially according to the color of each pixel. We use the color ratio $\frac{R}{R+B+G}$ based on pixel values in the RGB colorspace to differentiate between two colors of each pixel. After generating the two-dimensional (intensity–color ratio) calibration map, we determine the depth field for both the combined two-plume system and each separate plume. We conduct two non-rotating tests to determine the sensitivity of this two-dimensional thickness calibration to dilution and mixing. The technique is also validated with a known dye solution volume using both non-rotating and rotating control volume experiment. The technique is applied to the two-plume experiment. We calculate the bulge volume growth rate and the coastal current freshwater transport based on the measured layer depth field. Finally, we use the color ratio to determine the fraction of fluid at a given location in the plume originating from each sources.

## 2 Experimental setup

The experiments were performed in an annular rotating tank with $\boldsymbol{R} = 92$ cm and $\boldsymbol{r} = 22$ cm (Fig. 1a). The tank was mounted on a standing table, which was leveled such that the water level difference over one rotation is less than 0.1%. The table was rotating counter-clockwise throughout the experiment. The details of the rotating table facility are described in Horner-Devine (2006).

The experiment water tank was 25 cm deep and made of transparent Plexiglas, with a 0.5-cm-thick Plexiglas lid placed above it to minimize the wind shear stress. A 91 cm × 122 cm × 0.8 cm LED Edge-lit light panel (Luminous Film 2000 Lx daylight, 36.0 Watts) was placed under the clear water tank to provide a uniform light source. The difference in luminance from edge to center of the light panel is less than 2%. A sheet of Plexiglas with tracing film on top of it was attached between the light

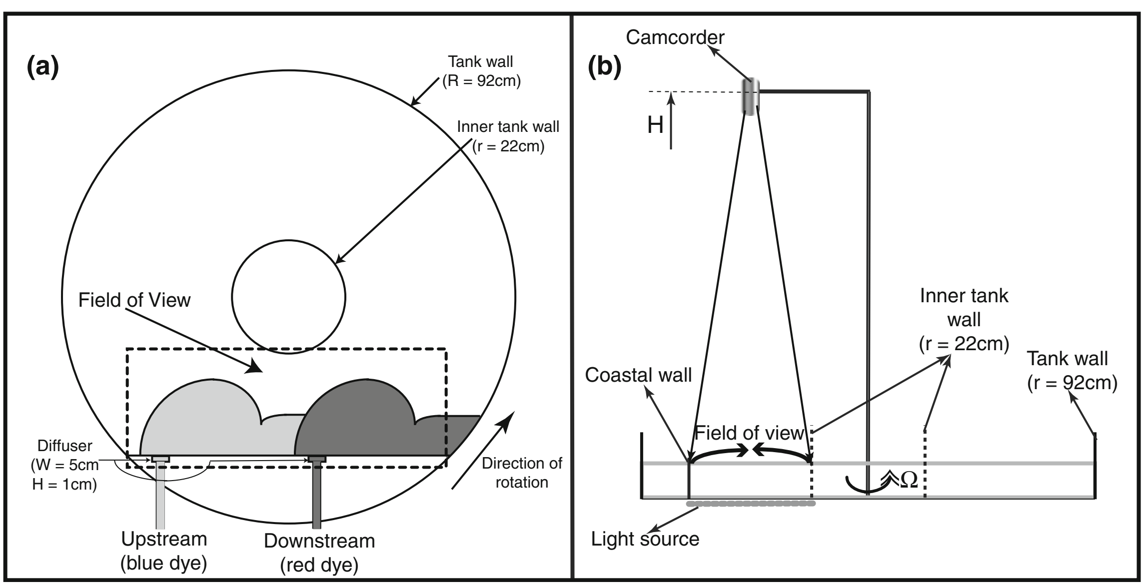


**Fig. 1** Schematic of the tank configuration viewed from above (**a**) and the rotating table viewed from the side (**b**)

source and the tank bottom to diffuse the light entering the tank and further improve its uniformity. This small variation was further corrected using a reference image taken before the experiment. Images were acquired using a Panasonic PV-GS320 3-CCD color video camera that was located 155 cm above the light panel and co-rotating with the water tank (Fig. 1b). The video camera operated at 30 frames per second with a resolution of 760 × 480 (horizontal by vertical) pixels. The 3-CCD color video camera measured the intensity of light in the R, G, and B color bands separately and saved it as digital data on MiniDV tapes. It should be noted that the algorithm used to generate the final RGB values that were recorded on the tape is inherently lossy, and the resolution of the system is somewhat degraded in this process.

Prior to each experiment, the tank was filled with salt water and allowed to achieve solid-body rotation by spinning up for 60 min, which is sufficiently larger than the homogeneous spin-up time scale $E^{-1/2}f^{-1} = 5$ min, where $E = \nu/fH^2$ is the Ekman number (Wedemeyer 1964). To generate the inflow fluids, 1 ml of pure food dye (deep blue and cherry red from ESCO FOODS Inc) was diluted to 2,000 ml using de-ionized (DI) water. The two sources of buoyant fluid were introduced into the tank just below the free surface of the ambient salt water through 5 cm × 1 cm diffuser boxes. Each diffuser consisted of a 6.25 cm$^3$ chamber filled with sponge to provide uniform outflow velocity distribution. They were affixed to the back of the coastal wall and separated by 18.7 cm. The flow rates were held constant by two identical magnetic drive centrifugal pumps (MARCH MFG INC, Model 893-001-03) and measured independently by two ball float flow meters (Key Instruments, 0 cm$^3$/s to 26.29 cm$^3$/s with 1.05 cm$^3$/s accuracy). The temperature of the buoyant source and the ambient tank water was measured before and during the experiments using a thermometer (DELTATRAK, −50°C to 200°C with 0.1°C accuracy), and the salinity was measured with a refractometer (Cole-Parmer EW-02940-41, 0–10% with 0.1% accuracy).

## 3 Measurement technique

To calculate the thickness field of the two-layer buoyant rotating gravity current, the two-dimensional calibration map was generated based on the measured intensity–thickness and color ratio–thickness relationships. The thickness calibration included five different red and blue dye ratios: pure red, pure blue, 1:1, 1:3, and 3:1 (hereafter referred to as red, blue, b1:r1, b1:r3, and b3:r1, respectively). Each thickness calibration was done by filling a wedge-shaped cuvette that was attached to the coastal wall in the tank before the experiment.

### 3.1 Intensity-thickness relation

As described in Cenedese and Dalziel (1998), Cenedese and Dalziel (1999), the dye attenuation theory derived from the classical Lambert–Beer Law gives the attenuation ratio

$$\frac{I(h,c)}{I_0(h,0)} = e^{-ach}, \tag{1}$$

where $I(h, c)$ is the transmitted intensity of light passing through a distance $h$ of fluid with dye concentration $c$, and $a$ is the attenuation coefficient. The effects of absorbed light by the tank bottom and lid, as well as the reflected light by various interfaces between different media, are minimized by normalizing the intensity of dyed water to the transmitted intensity for the same thickness of undyed water, $I_0(h,0)$, at each pixel.

For a dyed fresh buoyant layer on an undyed salty ambient water layer, the actual relationship is approximately exponential, but the asymptote is non-zero (Cenedese 1998)

$$\frac{I(h_1,c;h_2,0)}{I_0(H,0)} = e^{-ach_1} + b, \tag{2}$$

where $h_1$ and $h_2$ are the thicknesses of dyed buoyant and undyed salty water, respectively, $H = h_1 + h_2$ is the total water thickness, and $b$ is the asymptotic value of $I/I_0$ as the layer of dyed water thickness $h_1 \to \infty$ (i.e., $H \to \infty$). This relation was derived for monochrome image of a colored dye illuminated with white light. In our experiments, the color image is captured in a primitive RGB base, and the intensity is calculated by averaging the red, green, and blue values for each pixel (Gonzalez et al. 2004). This relation allows us to normalize the intensity of light transmitted through the two-layer system to a one-layer system with a total undyed thickness $H$ (Fig. 2a). This normalization is applied to each pixel in all images throughout the experiment. The background intensity $I_0$ is the reference image captured just before the fresh dyed water is injected into the tank.

### 3.2 Color ratio-thickness relation

In the two-dye experiment, it is necessary to differentiate between the blue and red water masses. Figure 2a suggests that the intensity–thickness relationships depend on dye colors. Therefore, the calibration uses a color ratio to define the relative color content at each point. We introduce a color ratio $Ci = \frac{R_n}{R_n+B_n+G_n}$ for this calibration, where $R_n$, $G_n$, and $B_n$ are the $R$, $G$, $B$ values normalized to the background $R_0$, $G_0$, $B_0$ values, respectively. In our experiments, the RGB color ratio was found more effective than other colorspace descriptions such as HSI, HSV, or Lab that we

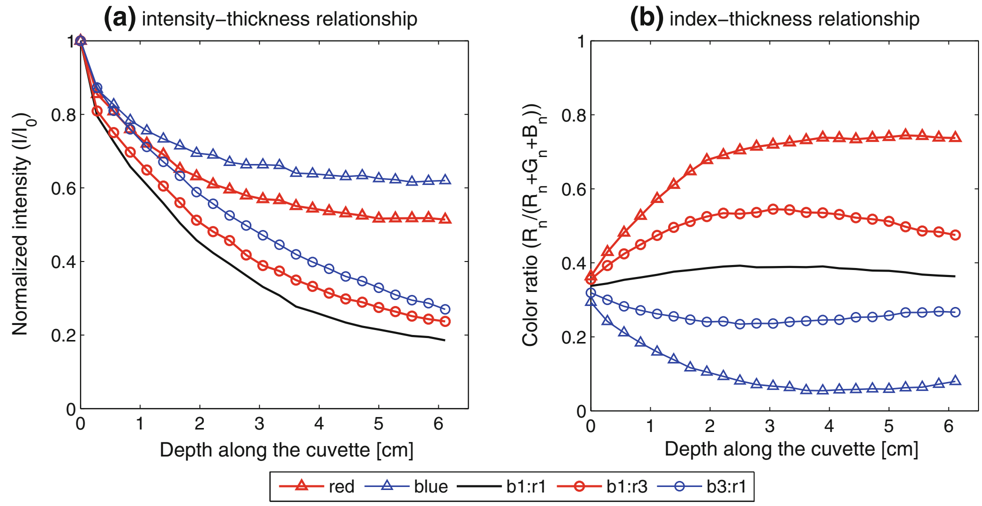


**Fig. 2** The layer thickness dependence of normalized intensity ($I/I_0$) for five different mixtures of *blue* and *red dye* solution (**a**) and the dependence of color ratio ($R_n/(R_n + G_n + B_n)$) for five different mixtures (**b**). All mixtures have $I/I_0 = 1$ at zero thickness and decay exponentially with increasing thickness (Eq. 2) with different attenuation coefficients

tested. The profile of the color ratio *Ci* along the cuvette varies nonlinearly with the thickness of the mixtures in cuvette (Fig. 2b). All five different mixtures have a color ratio =0.3333 at zero thickness because the no-dye image has equal values of $R_n$, $G_n$, and $B_n$. For thickness >0, the color ratio increases for the red and b1:r3 cases, decreases for the blue and b3:r1 cases and remains approximately constant for the 1:1 mixture. Finally, all the lines become approximately flat for thickness greater than 3 cm. The decrease or increase tendency of color ratios for larger thickness region is due to saturation of the R or B values. This does not have a significant effect on our experiments since the thickness is generally below 3 cm and can be avoided by further diluting the source dye.

We combined the intensity–thickness profiles (Fig. 2a) and color ratio-thickness profile (Fig. 2b) to develop a two-dimensional calibration map (Fig. 3). Thickness data were interpolated onto a 91 × 91 grid with intensity as abscissa, color ratio as ordinate, and thickness as color index.

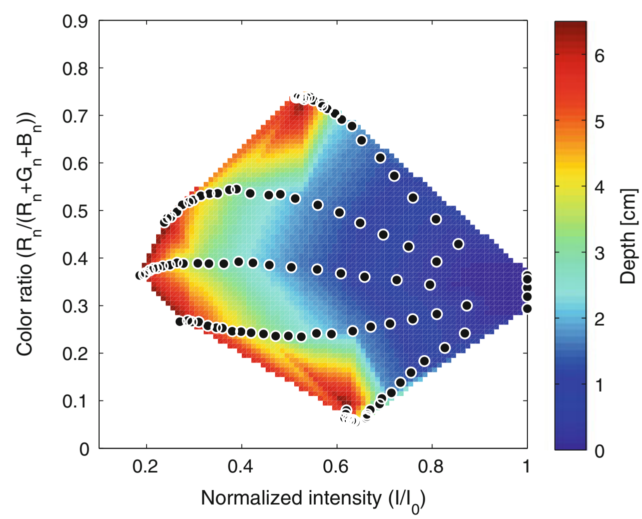


**Fig. 3** Two-dimensional (intensity–color ratio) calibration map generated from two thickness-dependent relationships, with intensity as abscissa, color ratio as ordinate, and thickness as color index. Color ratio versus normalized intensity of five different mixtures shown in Fig. 2 and used to generate the calibration map are also plotted in the figure

### 3.3 Buoyant water volume calculation

The depth field generated by two-dimensional calibration is used to calculate the freshwater volume in the buoyant layer. It is important to note that the optical thickness method measures the effective layer thickness, defined as

$$h_e = \frac{1}{C_0}\int C(z)\mathrm{d}z \simeq \frac{\bar{C}}{C_0}h_{real}, \qquad (3)$$

where $C$ and $C_0$ are the dye concentration in the plume and the source, respectively. Here, $\bar{C}$ is the vertically averaged dye concentration in the plume. In the two-plume system, mixing occurs both between the two dyed freshwater plumes and between each dyed freshwater plume and undyed salt water. The dye concentration is lower in the plume than in the source (i.e. $C < C_0$) because of mixing. Thus, the real thickness of dyed water in the tank is always larger than the effective thickness we measured, as the plume is continually diluted by entrained ambient salt water. However, since $h_e$ represents the amount of fresh water at each pixel location, it is the correct thickness for determining the volume of fresh water fluid masses. We calculated the total volume of fresh water by

$$V = \varepsilon \sum_{xpixels} \sum_{ypixels} (h_e), \qquad (4)$$

where $\varepsilon = 0.0112$ cm$^2$ is the area of each pixel.

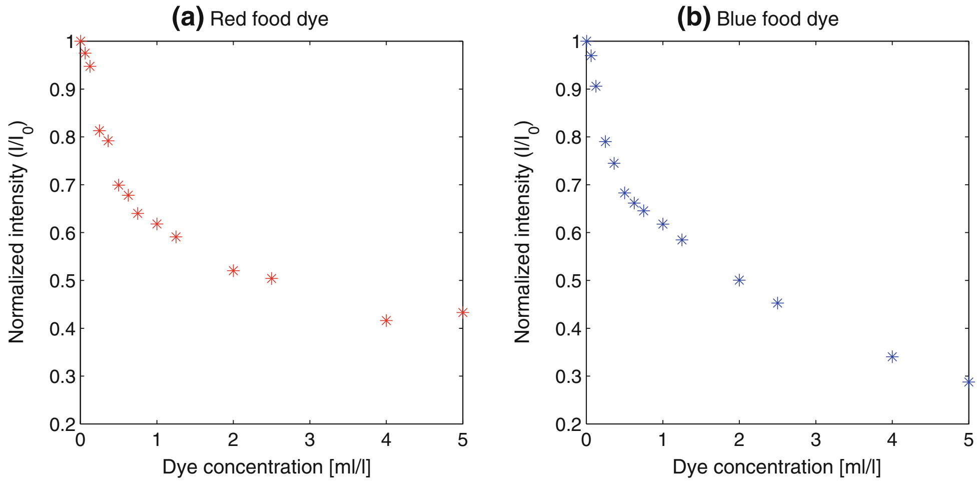


**Fig. 4** Relationship between normalized intensity ($I/I_0$) and the dye concentration for the red food dye (**a**) and the blue food dye (**b**)

## 4 Sensitivity and validation tests

### 4.1 Dilution sensitivity test

The optical thickness method is sensitive to the selected dye concentration because the intensity depends on the product of the dye layer thickness and the dye concentration. We conducted two tests to assess the sensitivity of the results to the dilution and hence optimize the selection of dye concentration. The normalized intensity decreases approximately exponentially with the increasing dye concentration for a fixed dye layer thickness of $h = 3.25$ cm (Fig. 4). Cenedese and Dalziel (1999) suggested a value $c_p$ as the maximum dye concentration, where the slope of the curve at $c_p$ is four times of the slope at $c = 0$. The dye concentration should be in the range of $0 < c < c_p$ to prevent a small error in normalized intensity leading to a large error in concentration. In our experiment, we determined $c_p = 1.04$ ml/l for red dye and $c_p = 1.60$ ml/l for blue dye. We selected a dye concentration $c = 0.5$ ml/l, which satisfied the above criteria for both dyes based on Eq. 27 in Cenedese and Dalziel (1999) with a maximum depth of 6 cm.

Another dilution test was designed to verify that the diluted calibration would provide more detailed information in a small range without changing the overall intensity–thickness relationship. We diluted the 0.5 ml/l dye water source at three different dilution factors: 1:1, 1:3, and 1:7. The normalized intensity against modified thickness plot shows a good agreement when each original thickness is divided by its corresponding dilution factor (Fig. 5). Therefore, the dilution does not affect the effective depth and the dyed water volume we are trying to calculate in our experiment.

### 4.2 Mixing sensitivity test

We used a cylinder mixing experiment to test the sensitivity of the two-color optical thickness method to mixing.

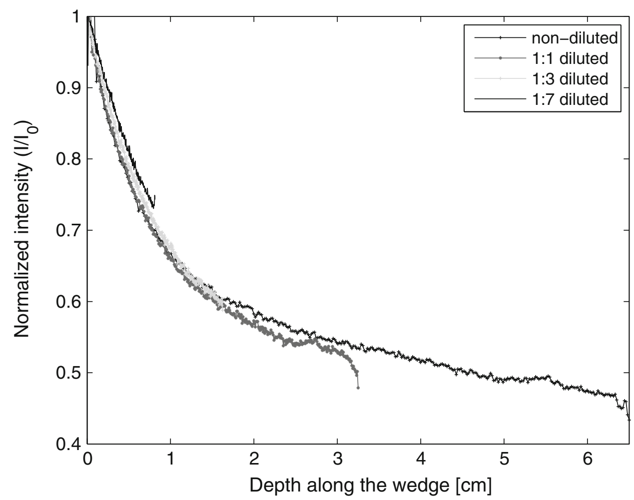


**Fig. 5** Red dye dilution test comparing non-diluted dye water to 1:1, 1:3, 1:7 DI water dilution. The normalized intensities $I/I_0$ are along the calibration wedge and depths for different dilutions are scaled by their corresponding dilution ratios

Equation 3 suggests that the effective thickness should remain unchanged before and after the mixing. This is because the product of the real depth and the dye concentration will not change based on the mass conservation, although they both changed separately. The experiment employed a Plexiglas bottomless cylinder supported by two blocks on the bottom so that the buoyant water in the cylinder cannot expand laterally, while the heavy salty water can exchange with the ambient water through the bottom. Selected volumes of fresh dye water were carefully introduced into the cylinder at the surface with a sponge end to minimize the initial mixing. We then used a piece of plastic plate to stir the surface-dyed water gently. We took images both before and after the mixing for comparison. The ratio of intensity after mixing to before mixing was selected as a quantitative criterion to determine whether mixing affected the effective thickness. We did the mixing test for both 0.5 and 3 cm thickness of blue- and red-dyed water. For all tests, the ratio was 1.0 with an average error of 0.61%.

### 4.3 Control volume cylinder test

We carried out two validation tests to determine the accuracy of the technique. The bottomless cylinder used in the mixing test was placed in a non-rotating water tank and partially filled with a known volume of buoyant dyed water to create a layer of known thickness over the salt ambient water. We used the dye concentration 1 and 0.5 ml/l (hereafter referred as non-diluted and diluted, respectively) in this test. We compared the thickness determined from the optical thickness technique with the known layer thickness to verify whether the measurement is accurate. For this calculation, the normalized intensity and color ratio were calculated from the cylinder RGB image for the 1cm by 1cm square at the center of cylinder. Then, the depth was determined by interpolation in the parameter space defined by Fig. 3 and averaged over the 1 cm$^2$ area. The calculated thicknesses based on the calibration map were plotted against the known thicknesses (Fig. 6). Note that the calculated thickness is outside of our calibration space for depth greater than 5 cm for some undiluted dye. Slight differences in the color ratio and intensity between the calibration cuvette images and the experimental field of view appear to shift these points out of range of the calibration parameter space in Fig. 3. For the remaining undiluted cases and the diluted cases, the calculated thickness shows good agreement to the known thickness, with the average error less than 10% for diluted dye and 20% for non-diluted dye. This is also consistent with the Cenedese and Dalziel (1999) criterion. A dye concentration of 0.5 ml/l is below the cutoff, while 1 ml/l is very near the cutoff which is expected a higher error in determining the layer thickness.

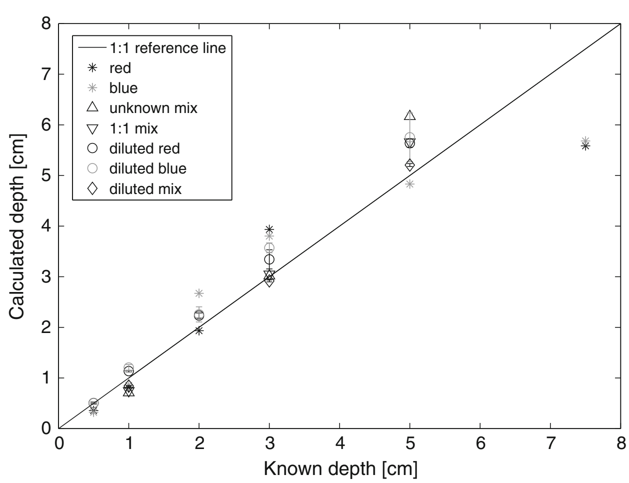


**Fig. 6** The cylinder layer thickness validation test with four non-diluted dyes (red, blue, unknown mix, 1:1 mix) and three diluted dyes (red, blue, mix). *Errorbars* are shown for the non-diluted dye cases. Many points with the layer thickness larger than 5 cm are missing because they are out of calibration map region

### 4.4 Rotating table volume test

A further test was devised to determine the ability of this technique to accurately measure the volume in a more complex flow, using the two-river experiment, as described in Sect. 2. In these experiments, inflow flow rate $Q$, table rotation period $T$, and reduced gravity $g'$ were varied. Here, $g' = \frac{\Delta\rho}{\rho_0}g$, where $\Delta\rho = \rho_0 - \rho$ is the density difference between the source and ambient water, $\rho_0$ is the density of the salty ambient water, $\rho$ is the density of fresh water, and $g$ is the gravitational acceleration. For the particular run discussed here, the upstream and downstream source flow rates were equal, at 8 cm$^3$/s, the rotation period was 15 s, and the reduced gravity $g'$ was 4.5 cm/s$^2$. We only considered the data from the first 25 s of the experiment, which was before the river plume left the camera's field of view. We calculated the total volume based on the measured depth field and compared it with the known inflow volume. The raw RGB image of the two plumes and the corresponding computed depth field at 25 s are shown in Fig. 7. The upstream (blue) plume enters the system through a diffuser between $x = 3.5$ cm to $x = 8.5$ cm, and the downstream (red) plume enters between $x = 27.2$ cm to $x = 32.2$ cm. The interaction of the two plumes will be discussed briefly in Sect. 5.

If we assume the layer thickness is constant within one pixel, the volume of each pixel equals the area of that pixel multiplied by its average depth. The total volume of freshwater in the two-plume system can be calculated from Eq. 4. This calculated volume should be equal to the volume of buoyant water discharged into the tank through both sources combined, which is given by

$$V_{in} = Q_{in}t. \tag{5}$$

The agreement between the measured plume volume and the freshwater input (Fig. 8) confirms that the method accurately accounts for the entire plume volume. The root mean squared error for the first 25 s is 6.41 cm$^3$, less than 4% of the total volume.

It is worth noting that this two-dimensional optical thickness technique may be sensitive to individual cameras. To address this question, we have recently introduced a research-grade single-CCD Bayer pattern camera (Point Grey Research Inc. GRAS-14S5C-C) for comparison. Although the pixel count on this camera is significantly higher than 3-CCD camera, the de-mosaicing of the Bayer information results in an effective pixel

**Fig. 7** Raw RGB video image (**a**) and depth field (**b**) generated from the two-dimensional calibration map of Run7 after 25 s. The *blue* and *red boxes* indicate the position of upstream and downstream sources, respectively

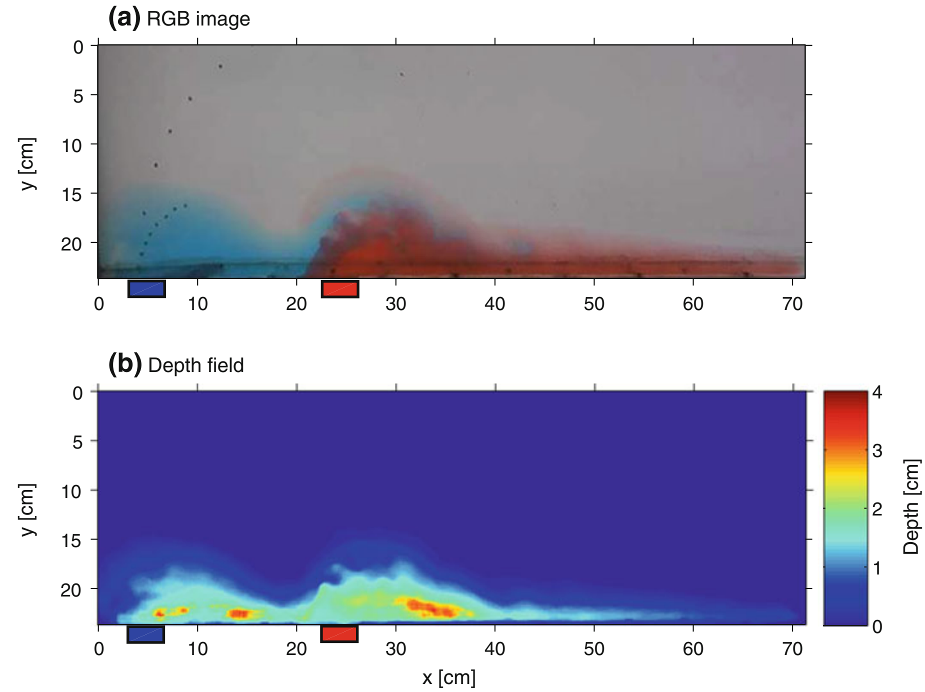


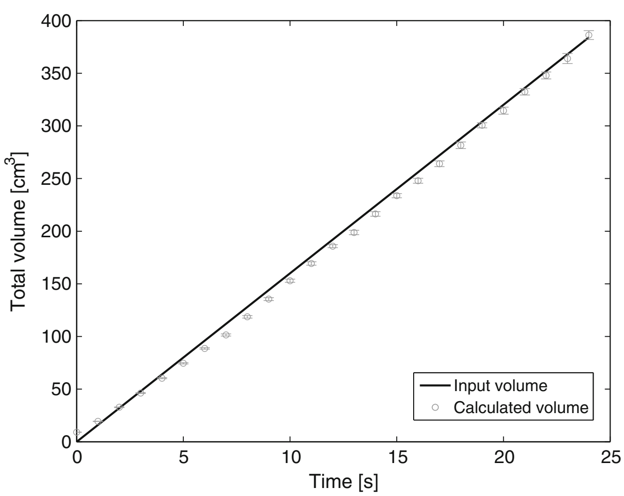


**Fig. 8** Comparison of the calculated total volume based on depth field (*circles*) to the total volume discharged into the tank (*black line*) before any buoyant fluid exits the view field ($0 \leqslant t \leqslant 25$ s). The rms error is less than 4%

resolution that is approximately the same as the 3-CCD camera. The research-grade camera is a 14-bit CCD, and so the resolution of the color information is finer, although the effective camera resolution is not as good as 14-bit. The comparison between two cameras suggests that the calibration maps are different case to case, especially for the larger layer thickness. Two calibration maps are consistent at the smaller thickness region, while the research-grade camera shows more variation in the deeper region. However, since most points in the plume are located in the shallower region, results from both the cameras satisfy the volume balance.

## 5 Application

In this section, we describe the application of the two-dimensional optical thickness method to the interaction of two river plumes in a two-layer rotating environment. As described in Sect. 2, blue and red dyes represented upstream and downstream fresh water rivers, respectively. Effective depth fields of both the red-dyed plume and blue-dyed plume were calculated, and the bulge volume and coastal current transport were subsequently determined from the depth field.

### 5.1 Separated bulge volume

One main purpose of the two-plume experiment is to test whether the downstream bulge volume reaches steady state due to the momentum flux from the upstream coastal current. To address this question, we calculate the downstream (red) bulge volume at various times. To evaluate the effective depth of each of the fluids in the mixing region, we assume their percentages vary linearly with the color ratio. Because there is some variation of color ratio in pure red and pure blue, we define the water with color ratio <0.3 as water that originated from the upstream source, with color ratio >0.5 as water that originated from the downstream source, and in between the percentage of the fluids from upstream increase linearly with the color ratio (Eq. 6)

$$h\%_{\text{downstream}} = \begin{cases} 0 & \text{if } Ci \leq 0.3; \\ 0.5 + 5 \times (Ci - 0.4) & \text{if } 0.3 < Ci \leq 0.5; \\ 1 & \text{if } Ci > 0.5. \end{cases} \tag{6}$$

The result of plume separation at 6T is shown in Fig. 9. The purple region between the two plumes may be explained by two possible reasons. First, it is the mixing region between the two plume. The interaction between the upstream coastal current and the downstream bulge has high mass exchange and then forms this mixing region. Alternatively, it may be due to the subduction of the upstream plume under the downstream plume, as described by the two-plume theory in Cenedese and Lerczak (2008). In their analytical model and laboratory experiments, the two river plumes tend to align vertically with the upstream coastal current underneath the downstream plume because the upstream fluid has more opportunity to mix with the higher-density ambient water. Viewed from above, it tends to be purple because a portion of upstream plume is covered by the downstream plume.

In order to compute bulge volume, we need to identify the region of the field of view occupied by the bulge and exclusive of the coastal current. This is somewhat complicated due to the fact that the bulge expands in the alongshore direction. We assume that the bulge has a linear alongshore growth rate and adjust the field of view for our image interrogation accordingly. For the upstream bulge, the situation is different because it would never continue to grow laterally because it hits the downstream plume. We calculated the upstream and downstream bulge volume separately based on Eq. 4 from their depth fields. Both plumes grow at exactly the same rate, and the sum of their volume is equal to the total entering freshwater volume (Fig. 10 insert).

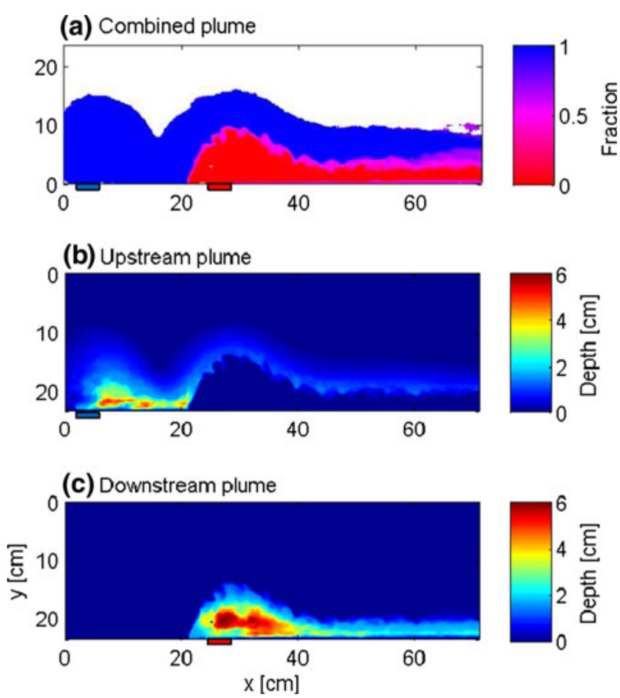


**Fig. 9** Discrimination of red and blue source fluid in the plume. Combined plumes showing fraction of blue source fluid at each pixel at $t = 6T$ (**a**), upstream (*blue*) plume depth field (**b**), and downstream (*red*) depth field (**c**). The purple region in **a** indicates the mixing region. The *blue* and *red boxes* indicate the position of upstream and downstream sources, respectively

## 5.2 Two river plumes' evolution

Six examples of two-plume evolution are shown in Fig. 11a–f, corresponding to $t = T$, $5T$, $10T$, $20T$, $30T$, and $37T$ ($T = 15$ s), respectively. The upstream plume reaches the downstream plume after $0.6T$, and the two plumes begin to interact with each other at the end of first period (Fig. 11a). After one rotation period, the downstream bulge tends to grow alongshore, while the upstream bulge tends to grow offshore and wrap around the downstream plume bulge (Fig. 11b, c). Later, the downstream bulge is sucked into the upstream bulge, forming a bigger re-circulating bulge. A small bulge separates from the big bulge and propagates downstream (Fig. 11d). This cycle continues, i.e. the big bulge accumulates the inflow fluid and becomes unstable, a small bulge separates from the big bulge and propagates downstream, then the big bulge returns to its stable state (Fig. 11e, f). It is interesting to note that fluid from the downstream source is drawn all the way to the upstream source and even appears to be entrained into the outer edge of the upstream plume (Fig. 11e). We also observe that the width of the band of

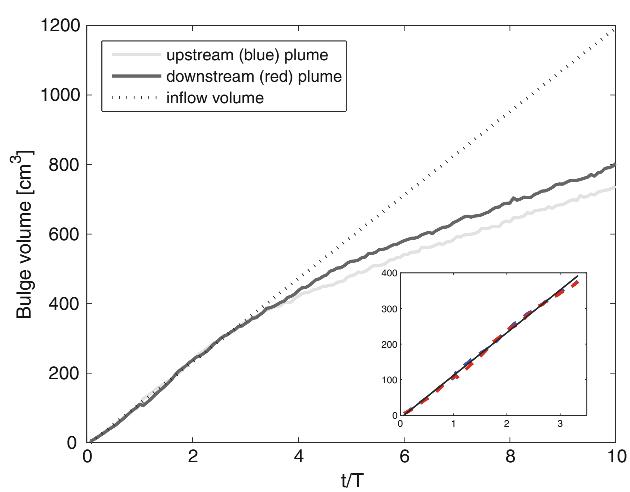


**Fig. 10** Upstream and downstream river bulge volume growth ($0 \leqslant t \leqslant 10T$) and comparison to the real inflow volume. The insert is the zoom-in of first $3.5T$. *Blue* and *red dashes* represent the upstream and downstream plume, respectively

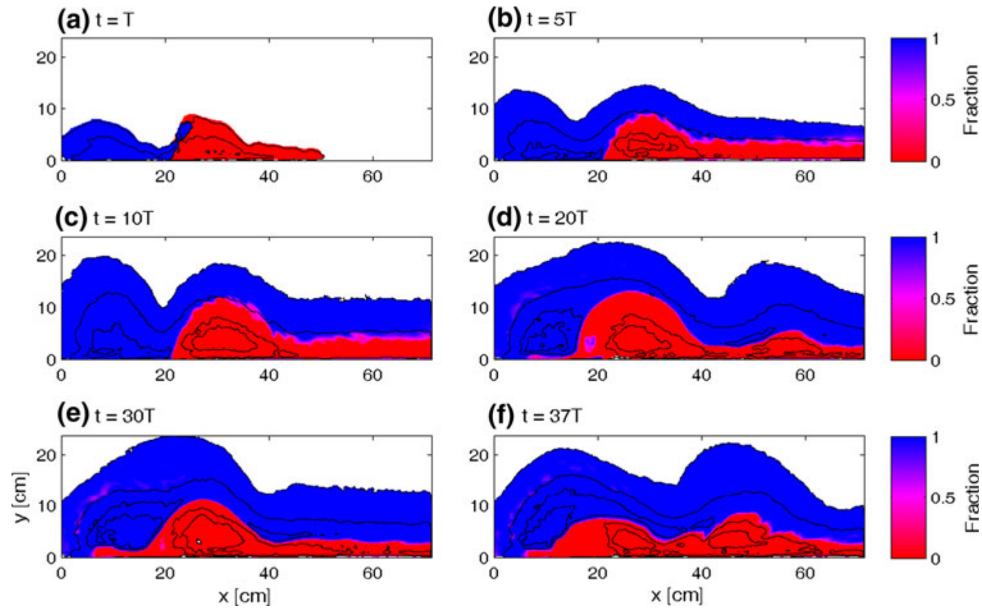


**Fig. 11** Fractional source content of two-plume system for run 7 at $t = T$ (**a**), $t = 5T$ (**b**), $t = 10T$ (**c**), $t = 20T$ (**d**), $t = 30T$ (**e**), and $t = 37T$ (**f**). The 0.05-, 1-, 3-, and 5-cm-depth contours are shown. *Blue* and *red boxes* indicate the position of upstream and downstream sources, respectively

mixed fluid between the two plumes increases around $t = 5 - 10T$ and then decreases afterward. The reasons for this will be investigated in future studies.

### 5.3 Coastal current transport

The coastal current in the river plume system is held to the wall due to Coriolis forces. The flow approaches a state of geostrophic equilibrium in which buoyancy and Coriolis forces are in balance and further release of potential energy is impossible (Griffiths 1986).

The alongshore velocity in the coastal current can be derived based on a two-layer model that has a quiescent lower layer and geostrophic cross-shore momentum balance. Thus,

$$u = -g\frac{\Delta\rho}{\rho_0 f}\frac{\partial h}{\partial y} = -\frac{g'}{f}\frac{\partial h}{\partial y}, \tag{7}$$

where $h$ is the buoyant plume thickness, $u$ is the alongshore velocity, $f$ is the Coriolis parameter. Note that $\rho$, $h$, $u$ are depth-averaged values, but they can vary as a function of $y$, the cross-shore distance. The alongshore coastal current transport can be calculated by integrating the velocity over the coastal current section area,

$$Q_{cc} \equiv \iint u\mathrm{d}A = \int_0^W \int_{-h}^0 u\mathrm{d}z\mathrm{d}y = \int_0^W -\frac{g}{f\rho_0}\frac{\partial \Delta\rho h}{\partial y}h\mathrm{d}y. \tag{8}$$

As suggested by Fong and Geyer (2002), a freshwater transport is defined based on the further assumption that the density anomaly is approximately proportional to the salinity anomaly, $\Delta\rho = \beta\Delta S$, where $\beta = 0.79$ kg m$^3$ psu$^{-1}$. Thus, the freshwater transport is

$$Q_{fcc} \equiv \iint u\frac{\Delta S}{S_0}\mathrm{d}A \approx \frac{1}{\beta S_0}\int_0^W \int_{-h}^0 u\Delta\rho\mathrm{d}z\mathrm{d}y$$
$$= \frac{1}{\beta S_0}\int_0^W -\frac{g}{f\rho_0}\frac{\partial(\Delta\rho h)}{\partial y}\Delta\rho h\mathrm{d}y. \tag{9}$$

Here, $h$ is the real plume depth including the initial fresh dyed water and the salty undyed water, which has been entrained into the plume during the mixing process. As discussed in Sect. 3, the measured effective depth is a function of the concentration ratio times the real depth (Eq. 3). Assuming that the water in the plume is well mixed, one can easily convert the concentration ratio to the density anomaly ratio

$$\frac{C}{C_0} = \frac{V_F}{V_T} = \frac{\Delta\rho}{\Delta\rho_{\max}}, \tag{10}$$

where $V_F$ and $V_T$ are the fresh water and total water volume, respectively, and $\Delta\rho_{\max}$ is the density difference between inflowing fresh water and ambient salty water, *i.e.* $\Delta\rho_{\max} = \rho_{ambient} - \rho_{inflow}$.

Substituting Eqs. 3 and 10 into Eq. 9, the freshwater transport is

$$Q_{fcc} = -\frac{g(\Delta\rho_{\max})^2}{\beta S_0 f\rho_0}\int_0^W \frac{\partial h_e}{\partial y}h_e\mathrm{d}y$$
$$= -\frac{g'_{\max}\Delta\rho_{\max}}{\beta S_0 f}\int_{h_e@(y=0)}^{h_e@(y=W)} h_e\mathrm{d}h_e, \tag{11}$$

where $g'_{\max}$ is the reduced gravity based on $\Delta\rho_{\max}$. For a given inflow and ambient salinity (density), the freshwater

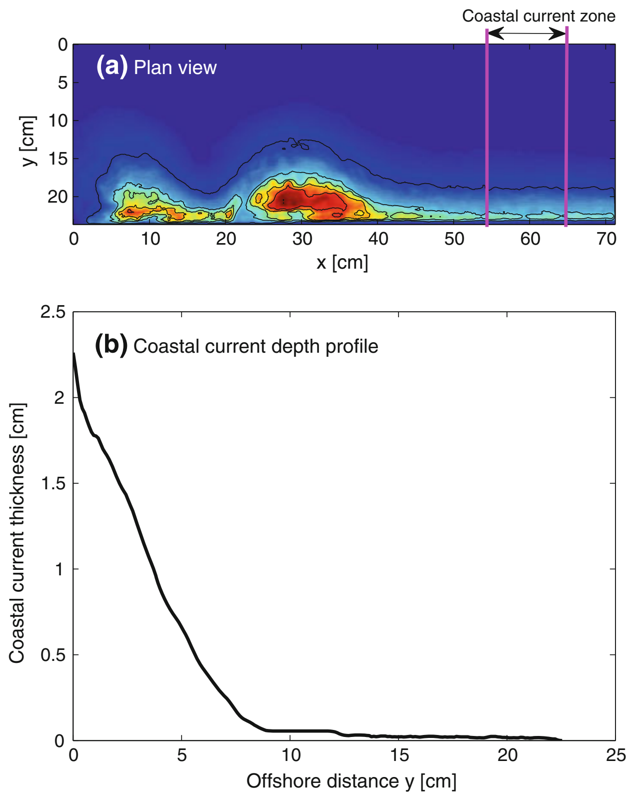


**Fig. 12** Two plumes depth field (**a**) at $t = 6T$. Cross-shore coastal current depth profile (**b**), averaging in $x$ direction from the coastal current zone shown in **a**

transport is only a function of the coastal current effective depth, $h_e$. From the measured coastal current effective depth field, we can calculate the freshwater transport by numerically integrating the effective depth over its entire width

$$Q'_{fcc} = -\alpha Q_{fcc} = -\alpha \frac{g'_{\max}\Delta\rho_{\max}}{\beta S_0 f}\sum_{i=1}^{N} h_e(i)[h_e(i+1) - h_e(i)], \tag{12}$$

where $\alpha$ is an $\mathcal{O}(1)$ empirical constant. We can then determine the value of $\alpha$ based on the total volume balance. The calculated coastal current transport with $\alpha = 1$ are shown in Fig. 13.

Theoretically, we can derive a freshwater mass conservation equation similar to the one in Sect. 4 . The volume of buoyant water discharged into the tank should be equal to the calculated plume volume within the camera field of view plus the freshwater transport out of view through the coastal current, expressed as

$$V_{in} = Q_{in}(t - t_0) = V_{field} + \sum Q'_{fcc}\Delta t. \tag{13}$$

For this case, the empirical constant $\alpha$ must be 0.6 to balance the flow into and out of control volume (Fig. 14). This relatively low empirical constant might be due to two

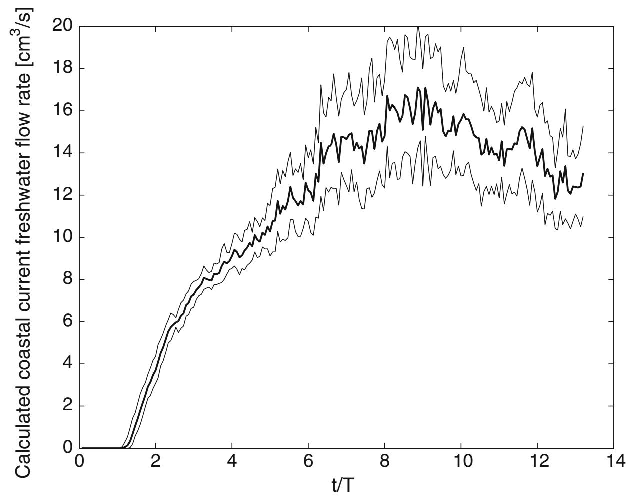


**Fig. 13** Freshwater coastal current transport computed by Eq. 12 with the empirical coefficient $\alpha = 1$ ($0 \leqslant t \leqslant 13T$) (*thick line*). Two *thin lines* represent the error bound, based on the standard deviation of coastal current depths

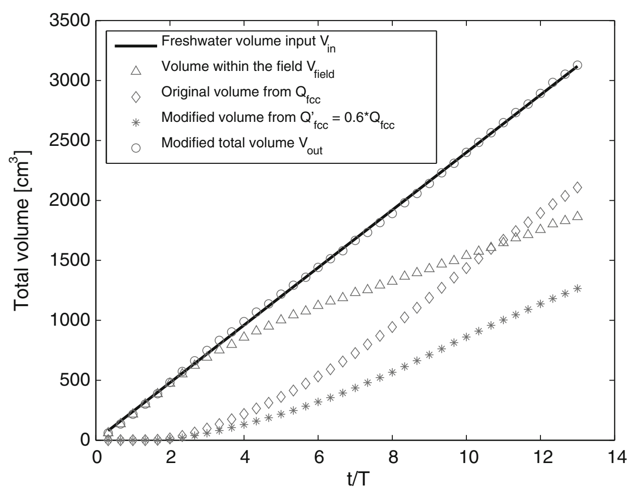


**Fig. 14** Total freshwater volume balance ($t$ = 0–13$T$). The total volume input (*black line*) is balanced by the total output (*circle*), which is the sum of volume within the field (*triangle*) plus the freshwater transport in the coastal current (*asterisk*). Note that the modified freshwater transport ($Q'_{fcc} = \alpha Q_{fcc}$) equals empirical coefficient ($\alpha = 0.6$) times the calculated freshwater transport [$Q_{fcc}$(*diamond*)]

possible reasons. Imaging of the region very near the coastal wall is degraded due to the presence of the bottom of the wall in the images. This may artificially increase the transport estimate. Another plausible explanation is that the two-layer system with a quiescent lower layer is not a proper assumption in this two-plume system if the interaction between two plumes is similar to scenario $\mathcal{A}$ in Cenedese and Lerczak (2008). In this case, it is actually a three-layer system with a quiescent bottom layer. The middle (blue) and upper (red) layer cannot be considered a simple geostrophic current together.

## 6 Conclusion

A modified optical thickness method is used to calculate the depth field of two interacting water sources by combining the reduction in intensity of transmitted light and the RGB color ratio of a dyed buoyant layer. A procedure to generate a two-dimensional calibration map from two depth-dependent relationships is presented. The measured depth field is used to calculate the total buoyant gravity current volume in the field of view. The technique is successful in measuring the dyed freshwater depth in a cylinder depth test with 10% average error. This technique was then applied to a two-plume experiment to measure the depth field of both plumes. Prior to the time that the plume water exits the field of view, the technique is successful in calculating the buoyant gravity current volume to within 4% error of prescribed volume input.

We also formulate an expression for the freshwater transport in the coastal current based on the obtained depth field and the assumption that the coastal current in a cross-shore geostrophic balance. The computed transport closes the freshwater budget for the system, but requires an empirical coefficient $\alpha = 0.6$. Although this coefficient is significantly below unity, the fact that the computed transport only departs from that needed to close the balance by a constant implies that our expression captures the principal dynamics of the system.

**Acknowledgments** We thank Peter B. Rhines for suggesting the optical thickness method, and Eric G. Lindahl, Bob Koon, Bertrand Dano, and Kris Skotheim for their support in re-building the rotating tank and development of the technique. YY acknowledges the support of the Endowed Presidential Fellowship. MEA acknowledges the support of William and Marilyn Conner Graduate Fellowship. This research was supported by NSF grant OCE-0850847.

## References

Afanasyev YD, Rhines PB, Lindahl EG (2009) Velocity and potential vorticity fields measured by altimetric imaging velocimetry in the rotating fluid. Exp Fluids 47(6):913–926

Avicola G, Huq P (2002) Scaling analysis for the interaction between a buoyant coastal current and the continental shelf: experiments and observations. J Phys Oceanogr 32(11):3233–3248

Cenedese C (1998) Baroclinic eddies over topography. PhD thesis, University of Cambridge

Cenedese C, Dalziel S (1998) Concentration and depth field determined by the light transmitted through a dyed solution. In: 8th international symposium on flow visualization, pp 61.1–61.5

Cenedese C, Dalziel S (1999) Concentration and depth fields determined by the light transmitted through a dyed solution. Exp Fluids (submitted)

Cenedese C, Lerczak JA (2008) Understanding the dynamics of the interaction between two river plumes. In: Fifth international symposium on environmental hydraulics, pp 1–6

Chant RJ, Glenn SM, Hunter E, Kohut J, Chen RF, Houghton RW, Bosch J, Schofield O (2008) Bulge formation of a buoyant river outflow. J Geophys Res 113:C01017. doi:10.1029/2007JC004100

Cowen EA, Chang KA, Liao Q (2001) A single-camera coupled PTV technique. Exp Fluids 31(1):63–73

Fong DA, Geyer WR (2002) The alongshore transport of freshwater in a surface-trapped river plume. J Phys Oceanogr 32(3):957–972

Gonzalez RC, Woods RE, Eddins SL (2004) Digital image processing using MATLAB. Prentice Hall, Englewood Cliffs

Griffiths R (1986) Gravity currents in rotating systems. Annu Rev Fluid Mech 18:59–89

Griffiths RW, Hopfinger EJ (1983) Gravity currents moving along a lateral boundary in a rotating fluid. J Fluid Mech 134:357–399

Holford JM, Dalziel SB (1996) Measurements of layer depth during baroclinic instability in a two-layer flow. Appl Sci Res 56(2-3):191–207

Horner-Devine AR (2006) Velocity, density and transport measurements in rotating, stratified flows. Exp Fluids 41(4):559–571

Horner-Devine AR (2009) The bulge circulation in the columbia river plume. Pergamon-Elsevier Science Ltd, Oxford, pp 234–251

Horner-Devine AR, Fong DA, Monismith SG, Maxworthy T (2006) Laboratory experiments simulating a coastal river inflow. J Fluid Mech 555:203–232

Linden PF, Simpson JE (1994) Continuous releases of dense fluid from an elevated point source in a cross-flow. In: Beven KJ, Chatwin PC, Millbank JH (eds) Mixing and transport in the environment. Wiley, New York, pp 401–408

Nof D, Pichevin T (2001) The ballooning of outflows. J Phys Oceanogr 31(10):3045–3058

Tian XD, Roberts PJW (2003) A 3D LIF system for turbulent buoyant jet flows. Exp Fluids 35(6):636–647

Wedemeyer E (1964) The unsteady flow within a spinning cylinder. J Fluid Mech 20:383–399

Zhang X, Dabiri D, Gharib M (1996) Optical mapping of fluid density interfaces: concepts and implementations. Rev Sci Instrum 67(5):1858–1868